Journal of the Mechanics and Physics of Solids 61 (2013) 1600–1611

Contents lists available at SciVerse ScienceDirect

Journal of the Mechanics and Physics of Solids

journal homepage: www.elsevier.com/locate/jmps

Effect of in-plane deformation on the cohesive failure of heterogeneous adhesives

Alejandro M. Aragón [a], Soheil Soghrati [b], Philippe H. Geubelle [a,*]

[a] Aerospace Engineering Department, University of Illinois, 104 South Wright Street, Urbana, IL 61801, USA
[b] Civil and Environmental Engineering Department, University of Illinois, 205 North Mathews Avenue, Urbana, IL 61801, USA

ARTICLE INFO

Article history:
Received 25 May 2012
Received in revised form
25 February 2013
Accepted 11 March 2013
Available online 29 March 2013

Keywords:
Cohesive modeling
Micro-to-macro analysis
Generalized/extended finite element method
Heterogeneous adhesives
Homogenization
Viscous damage model

ABSTRACT

The effect of in-plane deformations on the failure response of heterogeneous adhesives with a second phase of spherical elastic particles is investigated numerically using a 3D cohesive framework. The methodology includes a new interface-enriched generalized finite element scheme for the solution of structural problems with weak discontinuities, allowing for the efficient and accurate prediction of the stress and displacement fields in the adhesive based on finite element meshes that do not conform to the heterogeneities. A rate-dependent isotropic failure model is adopted to capture the failure in the matrix, while the stiff inclusions are assumed to be linearly elastic. Cohesive failure envelopes resulting from the micro-to-macro analysis are extracted for a wide variety of failure mode conditions. A study of 1611the impact of in-plane tensile and shear strains on the macroscopic failure response under tensile (mode I) loading is also presented.

1. Introduction

Heterogeneities are often introduced in adhesive layers to improve their failure properties and/or to provide additional functionalities. Zhao et al. (2000) showed that adding a glass fiber additive to an epoxy-based adhesive stabilized crack propagation in double cantilever beam (DCB) specimens. White et al. (2001) explored the autonomic healing capabilities of polymers containing a micro-encapsulated healing agent, and showed that up to 75% of the virgin fracture toughness could be recovered. Kinloch (2003) showed that adding rubber particles as a second phase in polymeric adhesives could greatly improve their fracture toughness. Dean et al. (2004) presented a numerical model for the study of these rubber-toughened polymers, considering the effect of rubber particle cavitation. Meguid and Sun (2004) showed that carbon nanotubes and alumina powder fillers in an epoxy adhesive improve up to certain point the debonding properties of the interface. Finally, Zhao and Hoa (2007) studied the effect of particle sizes in the toughening response of epoxy polymers, and provided a fracture model for their characterization. In all these and other related cases, adding heterogeneities in the adhesive layer leads to complex failure processes, including cavitation (Dean et al., 2004), particle or fiber debonding (Kawaguchi and Pearson, 2003), micro-crack nucleation (Guarino et al., 1999), propagation and coalescence (Ramanathan et al., 1997; Tang and Kou, 1998).

By collapsing the thin adhesive layer to a surface, cohesive modeling is a natural approach to analyze the failure response of bonded structures. Various cohesive models have been proposed over the past two decades based on a wide range

* Corresponding author. Tel.: +1 217 244 7648; fax: +1 217 244 0720.
E-mail addresses: alejandro.aragon@fulbrightmail.org (A.M. Aragón), ssoghra2@illinois.edu (S. Soghrati), geubelle@illinois.edu (P.H. Geubelle).

0022-5096/$ - see front matter © 2013 Elsevier Ltd. All rights reserved.
http://dx.doi.org/10.1016/j.jmps.2013.03.003

of phenomenological, and mathematically simple relations, the latter including polynomial (Needleman, 1990), bilinear (Geubelle and Baylor, 1998), exponential (Needleman, 1990; Ortiz and Pandolfi, 1999), and trapezoidal (Ferracin et al., 2003) expressions. Nevertheless, while these relations usually include some simplified model of the coupling between tension and shear failure in the case of mixed-mode loading, they do not include the effect of the tensile, compressive and/or shear deformations present in the plane of the adhesive layer. To provide a link between the macroscopic cohesive failure law and the microscopic detail of the failure processes, multiscale cohesive models have been recently proposed to impart a stronger physical basis to the traction–separation law used at the macroscale. The simulation of the failure response of heterogeneous adhesives can be traced back to the work of Matouš et al. (2008), who proposed a micro-to-macro cohesive framework to extract physically based traction–separation laws of adhesives. That work, which was performed in a 2D, plane strain setting and studied the effect of particle size and particle volume fraction for both hard-brittle and soft matrices, was extended by Kulkarni et al. (2009) to include particle-matrix decohesion at the microscale. The latter paper provided a study of representative volume element (RVE) sizes of 2D heterogeneous adhesives, the effects of particle size, volume fraction, and particle-matrix debonding parameters. Hirschberger et al. (2009) extended the work of Matouš et al. (2008) to include finite kinematics and provided numerical results without damage using an iterative nested procedure to fully couple both macro and micro scales within a two-level finite element (FE^2) setting. The multiscale failure response of 2D heterogenous adhesives in a fully coupled FE^2 setting under small strain assumptions was later presented by Kulkarni et al. (2010), who verified the multiscale cohesive framework through an adhesive patch test, which was compared with the results of direct numerical simulation (DNS), and provided also mode I and II failure simulations for a DCB specimen. Similar results were reported by Nguyen et al. (2011), who showed the existence of a RVE for quasi-brittle materials with heterogeneous microstructures, using also the FE^2 computational homogenization approach and DNS verification. Coenen et al. (2011, 2012) investigated the effect of boundary conditions and provide a methodology for imposing boundary conditions at the microstructure that results in a more realistic damage pattern. The DNS of the transverse failure response of fiber-epoxy systems was investigated by Cid Alfaro et al. (2010) using an interface-damage model to describe both the failure process within the epoxy and the fiber debonding. Finally, Nguyen et al. (2012) modeled in a FE^2 setting the macroscale crack response based on the damage of a heterogeneous microstructure.

This manuscript builds on the 2D one-way coupling cohesive framework introduced by Matouš et al. (2008) and investigates the cohesive failure response of an epoxy adhesive layer reinforced by stiffer spherical elastic particles. The focus of the present study is twofold. Firstly, the micro-to-macro analysis is performed in a fully 3D setting and therefore captures more accurately the complex failure process taking place in the particulate adhesive layer. Secondly, the analysis presented hereafter focuses on modeling the effect of tensile and shear deformation present in the plane of the adhesive layer on the macroscopic failure response, i.e., the resulting traction–separation law. The issue of the contribution of in-plane stretches has also been addressed in a recent publication by McBride et al. (2012), who proposed a unifying cohesive homogenization formulation for heterogeneous adhesives. In the present study, the analysis of a heterogeneous adhesive is performed through a nonlinear finite element model. To facilitate the modeling of the complex microstructure and allow for an efficient treatment of multiple realizations of the particle distributions, we adopt the Interface-enriched Generalized Finite Element Method (IGFEM), which allows for the decoupling of the finite element discretization from the details of the microstructure (Soghrati et al., 2011). This novel GFEM scheme, which has been introduced for the solution of thermal problems in complex materials and structures, is used here in the micro-to-macro prediction of the constitutive and failure response of a heterogeneous solid.

The manuscript is organized as follows: Section 2 summarizes the formulation of the two-scale cohesive framework, followed in Section 3 by a presentation of the Interface-enriched GFEM formulation. The cohesive failure response of a heterogeneous solid in the absence of in-plane deformations is provided in Section 4, with emphasis on extracting the cohesive failure envelope under a wide range of mode mixity. Finally, the impact of in-plane deformations on the mode I cohesive failure law is investigated in Section 5.

2. Micro-macro formulation

Consider the bonded structure $\Omega \subset \mathbb{R}^3$ with closure $\overline{\Omega}$, described by the macroscopic coordinate $\mathbf{x}$ and shown schematically in Fig. 1. Based on the fact that the thickness l_c of the adhesive layer is much smaller than the other dimensions of the layer, the adhesive is represented by the (cohesive) surface Γ_c. Under this idealization, the interface Γ_c can be thought of as a lower-dimension manifold of zero measure such that $\overline{\Omega} = \overline{\Omega}^+ \cup \overline{\Omega}^-$. The domain boundary $\partial\Omega = \overline{\Omega} \backslash \Omega$ is divided into two mutually exclusive regions $\partial\Omega_u$ and $\partial\Omega_t$, where Dirichlet and Neumann boundary conditions are prescribed, respectively.

Given a macroscopic point $\mathbf{x}$ located on the adhesive surface Γ_c, let us introduce the periodic unit cell (PUC) Θ of the heterogeneous adhesive described by the microscale coordinate $\mathbf{y}$ (with y_3 aligned with the normal $\mathbf{n}$ to the adhesive surface) and schematically shown in the inset of Fig. 1. Relating the two scales through the asymptotic scaling parameter ξ, such that $\mathbf{x} = \xi \mathbf{y}$, we write the classical two-scale expansion of the displacement field as

$$\mathbf{u}(\mathbf{x}, \mathbf{y}) \approx \mathbf{u}(\mathbf{x}) + \xi\, {}^{\mu}\mathbf{u}(\mathbf{y}), \tag{1}$$

where $\mathbf{u}$ represents the macroscopic displacement that is uniform over the unit cell, and ${}^{\mu}\mathbf{u}$ the microscopic perturbation displacement. As in Eq. (1), all microscopic quantities are denoted henceforth with a left superscript μ.

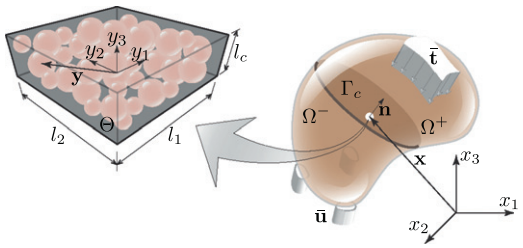

Fig. 1. Schematic of the two-scale cohesive boundary value problem. A macroscopic domain $\Omega \subset \mathbb{R}^3$ contains the thin heterogeneous adhesive layer Γ_c, whose unit cell associated with a macroscopic point $\mathbf{x}$, and periodic in the y_1 and y_2 directions, is illustrated in the inset.

In the micro-to-macro cohesive analysis presented hereafter, the macroscopic in-plane strains $\varepsilon_{\alpha\beta}$ (with $\alpha,\beta=1,2$) are defined on the cohesive surface Γ_c and the displacement jump vector $[\![\mathbf{u}]\!]$ across Γ_c is assumed to be known. Based on a linear kinematic assumption, the macroscopic strain tensor in the adhesive layer takes the form (Matouš et al., 2008):

$$\boldsymbol{\epsilon} = \begin{bmatrix} \varepsilon_{11} & \varepsilon_{12} & [\![u_1]\!]/2l_c \\ \varepsilon_{21} & \varepsilon_{22} & [\![u_2]\!]/2l_c \\ [\![u_1]\!]/2l_c & [\![u_2]\!]/2l_c & [\![u_3]\!]/l_c \end{bmatrix}, \tag{2}$$

The strong form of the boundary value problem at the micro-scale can then be written as

$$\nabla \cdot {}^{\mu}\boldsymbol{\sigma} = \mathbf{0} \quad \text{on } \Theta, \tag{3}$$

where ${}^{\mu}\boldsymbol{\sigma} = {}^{\mu}\boldsymbol{\sigma}(\boldsymbol{\epsilon} + {}^{\mu}\boldsymbol{\epsilon})$ is the stress field in the PUC, and ${}^{\mu}\boldsymbol{\epsilon} = \nabla^s_{\mathbf{y}}\,{}^{\mu}\mathbf{u}$ is the microscopic strain tensor with $\nabla^s_{\mathbf{y}}$ denoting the symmetric gradient operator on the PUC. As described in Matouš et al. (2008), periodic boundary conditions are imposed along the lateral surfaces of Θ on the microscopic displacement field ${}^{\mu}\mathbf{u}$, which is assumed to vanish along the top and bottom surfaces of the PUC. For a more general description of the kinematics of the cohesive surface and the contribution of the in-plane stretches, refer to McBride et al. (2012).

Following the methodology presented by Matouš et al. (2008) and Kulkarni et al. (2009, 2010), the microscale formulation is completed by an irreversible isotropic damage model used to capture the progressive degradation of the adhesive. Denoting the total potential energy function of the undamaged material at the microscale by

$$Y(\boldsymbol{\epsilon} + {}^{\mu}\boldsymbol{\epsilon}) = \tfrac{1}{2}(\boldsymbol{\epsilon} + {}^{\mu}\boldsymbol{\epsilon}) : {}^{\mu}\boldsymbol{\sigma}, \tag{4}$$

damage is introduced using a monotonically increasing damage parameter $\omega, (0 \le \omega \le 1)$, such that the stored energy in the damaged material is given by $(1-\omega)Y(\boldsymbol{\epsilon} + {}^{\mu}\boldsymbol{\epsilon})$. An approach similar to the yield surface in the theory of plasticity is then used to define the onset of damage in the material

$$g(Y,\chi^t) = G(Y) - \chi^t \le 0, \quad t \in \mathbb{R}^+, \tag{5}$$

$$G(Y) = 1 - e^{-((Y-\overline{Y})/p_1\overline{Y})^{p_2}}, \tag{6}$$

where χ^t is the state variable that keeps track of damage, and $G(Y)$ is the Weibull distribution function chosen to describe the process of damage. In the latter, $\overline{Y}$ is the energy threshold, and p_1, p_2 are the distribution parameters that adjust the scale and the shape of the function $G(Y)$, allowing for the modeling of a wide range of constitutive and failure responses. Viscous regularization, first introduced by Simo and Ju (1987a,b), is also used to avoid issues related to the mesh bias introduced by the damage model. Further details can be found in Matouš et al. (2008) and Kulkarni et al. (2009).

From the microscale solution, the cohesive traction acting along the cohesive surface Γ_c is readily computed as

$$t_i = \frac{1}{|\Theta|}\int_{\Theta} {}^{\mu}\sigma_{3i}(\boldsymbol{\epsilon} + {}^{\mu}\boldsymbol{\epsilon})\, d\Theta, \tag{7}$$

where the macroscopic strain tensor $\boldsymbol{\epsilon}$ is given by Eq. (2) and $|\Theta|$ denotes the volume of the PUC. Similarly, the macroscopic in-plane traction components $S_{\alpha\beta}$ defined on Γ_c as the energetic conjugate of the aforementioned surface strains $\varepsilon_{\alpha\beta}$ are obtained as

$$S_{\alpha\beta} = \frac{l_c}{|\Theta|}\int_{\Theta} {}^{\mu}\sigma_{\alpha\beta}(\boldsymbol{\epsilon} + {}^{\mu}\boldsymbol{\epsilon})\, d\Theta. \tag{8}$$

The link between the macroscopic quantities defined on Γ_c (cohesive traction $\mathbf{t}$, displacement jump $[\![\boldsymbol{u}]\!]$, in-plane tractions $S_{\alpha\beta}$, and strains $\varepsilon_{\alpha\beta}$) and the microscopic stress ${}^{\mu}\sigma$ and displacement ${}^{\mu}\mathbf{u}$ fields defined in the PUC can be obtained by equating their respective contributions to the virtual work as (Hill's lemma)

$$\frac{l_c}{|\Theta|}\int_{\Theta} {}^{\mu}\sigma_{ij}\,\delta(\boldsymbol{\epsilon}_{ij} + {}^{\mu}\boldsymbol{\epsilon}_{ij})\, d\Theta = t_i\,\delta\,[\![u_i]\!] + S_{\alpha\beta}\delta\varepsilon_{\alpha\beta}. \tag{9}$$

This relation, together with the equilibrium equations at the macroscale, would complete the fully coupled multiscale formulation, and its implementation in a FE^2 setting (Kulkarni et al., 2010).

3. Nonlinear interface-enriched GFEM implementation

As indicated in the introduction, a key element to this numerical study is the Interface-enriched Generalized Finite Element Method, introduced recently by Soghrati et al. (2011) and Soghrati and Geubelle (2012). Similar to the conventional GFEM, this method aims at providing an accurate and efficient finite element approximation in problems with weak discontinuities, i.e., problems where the gradient of the field is discontinuous along the phase interfaces, using finite element discretizations that do not conform to these interfaces. This property is particularly useful in 3D where the creation of conforming meshes can be complex,[1] time consuming or even not possible, especially when investigating multiple realizations of the microstructure to extract some statistics on the two-scale results as done later in this study. Optimal convergence rates are obtained by enriching the solution field in elements cut by a discontinuity interface to capture the information otherwise missing in the standard FEM approximation. For a given set of n Lagrangian shape functions $\{N_i(\mathbf{y}) : \mathbf{y}(\Theta) \to \mathbb{R}\}_{i=1}^{n}$, and m enrichment functions $\{\psi_i(\mathbf{y}) : \mathbf{y}(\Theta) \to \mathbb{R}\}_{i=1}^{m}$, the IGFEM approximation of the solution field at the microscale is given by

$$^{\mu}\mathbf{u}^h(\mathbf{y}) = \sum_{i=1}^{n} N_i(\mathbf{y})\overline{\mathbf{U}}_i + \sum_{i=1}^{m} s\psi_i(\mathbf{y})\hat{\mathbf{U}}_i, \tag{10}$$

where $\overline{\mathbf{U}}_i$ and $\hat{\mathbf{U}}_i$ are the standard and generalized degrees of freedom, respectively, and s is a scale factor employed to avoid sharp gradients in the enrichment functions for cases where the interface happens to pass close to a node of the non-conforming mesh (Soghrati et al., 2011). The first term in Eq. (10) corresponds to the standard FE portion of the approximation, while the second term adds the contribution of the enrichment function in capturing the gradient discontinuity along the phase interface.

To evaluate the enrichment functions associated with each interface node, we first divide the elements cut by the interface into the minimum number of sub-elements needed for an accurate quadrature in a non-conforming mesh. These elements, as in the conventional GFEM, are referred to as *integration elements*. Depending on the orientation of the interface, a non-conforming tetrahedral element is then divided into a combination of tetrahedral and wedge sub-elements that conform to the geometry of the interface. The enrichment functions are then obtained as a linear combination of the Lagrangian shape functions of the integration elements, which are able to model appropriately the discontinuous gradient field inside the parent element.

A major difference between the IGFEM and the conventional GFEM relies on the fact that the IGFEM does not use the *partition of unity* property (i.e., $\sum_{i=1} N_i = 1$) to localize the enrichment functions to the enriched nodes. The use of this property in the GFEM is important to ensure that the sparsity of the final stiffness matrix is preserved, as multiplying the enrichment function by the partition of unity causes the resulting function to vanish outside the cloud of elements surrounding the enriched node. The partition of unity is not used in the IGFEM, for the enrichment function vanishes by construction at the edges that do not interact with the phase interface. This feature also eliminates the need to introduce a correction function due to parasitic terms that appear in blending elements with certain choices of enrichment functions (Fries, 2008). Another key advantage of the IGFEM is concerned with the application of Dirichlet boundary conditions. While in the conventional GFEM the imposition of Dirichlet boundary conditions requires special treatment by using the penalty method, Lagrange multipliers, or even other methods (Babuška et al., 2003), this type of boundary conditions is imposed in a straightforward fashion within the IGFEM at the nodes created along the boundary due to the non-matching interfaces.

3.1. Finite element implementation

Consider a discretization of the microscopic domain Θ into $\mathcal{E}$ finite elements Θ_e such that $\bigcup_{e=1}^{\mathcal{E}} \overline{\Theta}_e \equiv \overline{\Theta}^h \cong \overline{\Theta}$, with discretized boundary $\partial\Theta^h \equiv \overline{\Theta}^h \backslash \Theta^h \cong \partial\Theta$. The resulting non-linear system of equations is solved numerically by the Newton–Raphson scheme, with the i-th iteration of the convergence loop written as (Matouš et al., 2008)

$$\mathbf{K}(^{\mu}\mathbf{U}_n^i, \boldsymbol{\epsilon}_n)\Delta^{\mu}\mathbf{U}_n^i = -\mathbf{R}(^{\mu}\mathbf{U}_n^i, \boldsymbol{\epsilon}_n), \tag{11}$$

where n denotes the loading step, $\boldsymbol{\epsilon}_n$ the corresponding imposed macroscopic strain given by Eq. (2), $\Delta^{\mu}\mathbf{U}_n^i$ the incremental microscopic nodal displacement vector and

$$\mathbf{K}(^{\mu}\mathbf{U}_n^i, \boldsymbol{\epsilon}_n) = \mathop{\mathbb{A}}_{e=1}^{\mathcal{E}} \mathbf{k}_e, \quad \mathbf{k}_e = \int_{\Theta_e} \left[(1-\omega_n^i)\mathbf{B}^T\mathbf{C}\mathbf{B} - \mathbf{B}^T {}^{\mu}\boldsymbol{\sigma}_n^i \otimes \frac{\partial \omega_n^i}{\partial {}^{\mu}\mathbf{U}_n^i} \right] d\Theta, \tag{12}$$

[1] *Conforming mesh* and *matching mesh* are used interchangeably in this paper, indicating that the edges of finite elements in the mesh are aligned with phase interfaces.

$$\mathbf{R}({}^{\mu}\mathbf{U}_n^i, \boldsymbol{\epsilon}_n) = \mathop{\mathbb{A}}_{e=1}^{\mathcal{E}} \mathbf{r}_e, \quad \mathbf{r}_e = \int_{\Theta_e} (1-\omega_n^i)\mathbf{B}^{T\,\mu}\boldsymbol{\sigma}_n^i \, d\Theta. \tag{13}$$

In Eqs. (12) and (13), $\mathbb{A}$ denotes the finite element assembly operator, $\mathbf{B}$ is the strain-displacement matrix, $\mathbf{C} = \partial^{\mu}\boldsymbol{\sigma}/\partial\boldsymbol{\epsilon}$ is the constitutive tangent tensor and ω is the damage parameter introduced in Section 2. The relation $\partial\omega/\partial^{\mu}\mathbf{U}$ can be obtained noting that the damage parameter is a function of the damage energy release rate, which in turn depends on the strain, i.e.,

$$\frac{\partial\omega_n^i}{\partial^{\mu}\mathbf{U}_n^i} = \frac{\partial\omega_n^i}{\partial\overline{Y}_n^i}\frac{\partial\overline{Y}_n^i}{\partial^{\mu}\boldsymbol{\epsilon}_n^i}\frac{\partial^{\mu}\boldsymbol{\epsilon}_n^i}{\partial^{\mu}\mathbf{U}_n^i}. \tag{14}$$

It is worth noting that, in the IGFEM, the size of the element local stiffness matrices $\mathbf{k}_e$ and residual vectors $\mathbf{r}_e$ of intersected elements is increased due to the generalized degrees of freedom. To solve for the incremental displacement $\Delta^{\mu}\mathbf{U}_n^i$ in Eq. (11), we use an adaptive load stepping scheme where the magnitude of the increment depends on the history of convergence.

3.2. Verification

Detailed convergence studies presented in Soghrati et al. (2011), Soghrati and Geubelle (2011) have demonstrated that, for linear heat transfer problems, the IGFEM possesses the same convergence rate and precision as the conventional FEM without the need of conforming meshes. To verify the extension of the IGFEM to nonlinear structural problems considering damage, we perform a volumetric micro-to-macro analysis on a simple PUC composed of a single embedded particle subjected to a uniaxial state of macroscopic strain (Fig. 2). The edge of the cubic PUC has a length $l = 1$ mm and the particle has a 500 μm diameter and is off-centered along the x-axis by 125 μm. Fig. 2 also shows details of the IGFEM and FEM meshes used in the comparison, with the matrix clipped at the center of the spherical inclusion for visualization purposes. The spherical particle shown in Fig. 2b is the result of the IGFEM interaction between the structured finite element mesh and the object that represents the inclusion. It is worth noting the smaller mesh size close to the particle in the matching mesh used in the solution of the standard FEM. Table 1 summarizes the elastic and volumetric damage properties of the compliant particle and the stiffer matrix. For the viscous regularization, a viscous parameter of 100 s^{-1} is chosen for this verification study.

Fig. 3a presents a direct comparison of the homogenized uniaxial stress–strain curves obtained with the standard FEM and the IGFEM, showing excellent agreement between the two analyses. This agreement extends not only to the stress-strain curves, but also to the details of the damage distribution after the peak load (Fig. 3b and c) and at the end of the simulation (Fig. 3d and e).

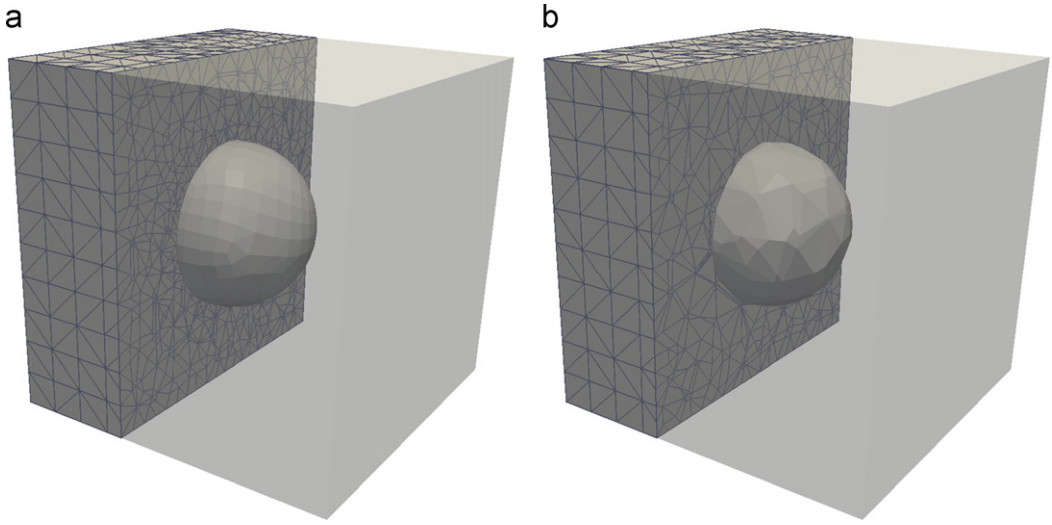

Fig. 2. Finite element meshes used for the single particle PUC verification study: (a) matching mesh used by the standard FEM; (b) non-conforming structured mesh used by the IGFEM.

Table 1
Material properties used in the verification problem shown in Fig. 2.

	E(GPa)	ν	$\overline{Y}$ (kPa)	p_1	p_2
Particle	3.9	0.33	4	100	1
Matrix	210.0	0.3	10	100	1

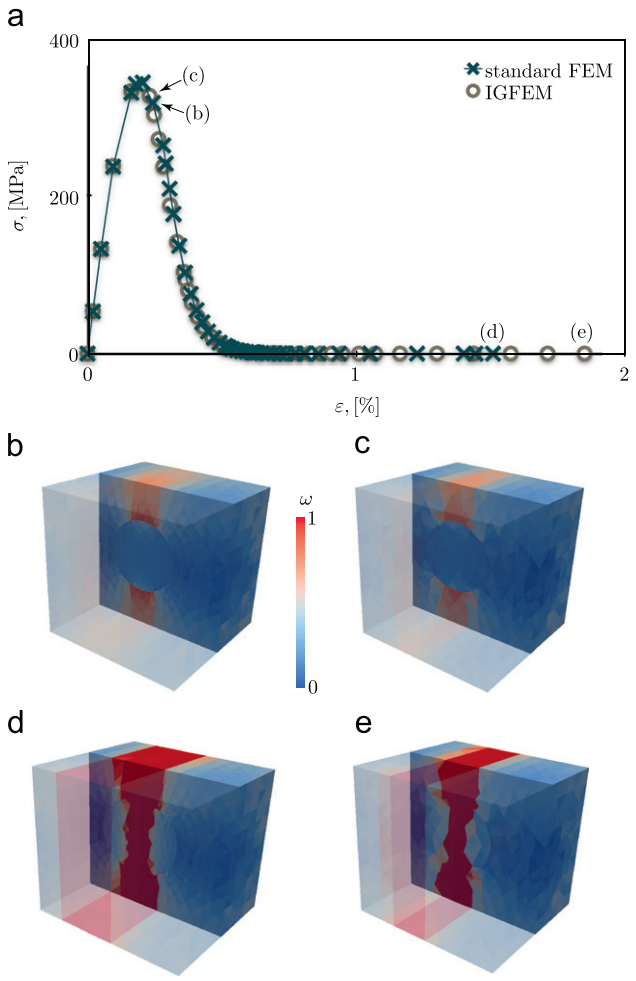

Fig. 3. Comparison between the standard FEM and the IGFEM for the volumetric micro-to-macro analysis described in Section 3.2. (a) Resulting macroscopic strain–stress curves; Damage distribution after the peak load (Fig. (b) and (c)) and at the end of the simulation (Fig. (d) and (e)) for the standard FEM and for the IGFEM, respectively.

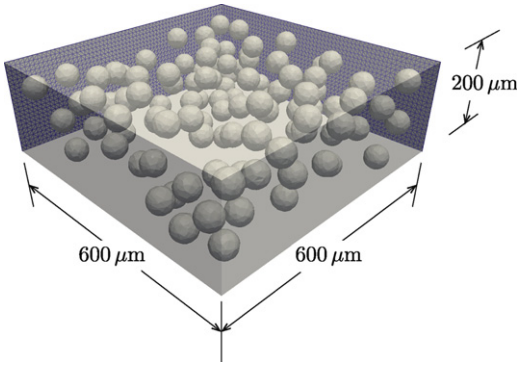

Fig. 4. (a) Geometry and particle distribution for a particular adhesive PUC.

4. Cohesive failure response in the absence of in-plane deformation

In this section, we apply the micro-to-macro cohesive formulation to extract the cohesive failure response of the heterogeneous adhesive shown in Fig. 4. The dimensions of the PUC, $l_1 = l_2 = 600$ μm and $l_c = 200$ μm, are chosen based on the results of a PUC size study conducted by Kulkarni et al. (2009), which indicated that a 3:1 length to thickness ratio was sufficient in this type of analysis to ensure the independence of the macroscopic traction–separation law on the PUC size.

The PUC contains 10% volume fraction of stiff elastic particles, totaling 110 particles with a diameter of 50 μm distributed randomly in the adhesive layer. The random particle distribution was obtained using the packing algorithm that serves as the foundation of the ROCPACK code used for the generation of realistic virtual packs of convex-shape particles (Stafford and Jackson, 2010). The constitutive properties of the particles and the matrix are listed in Table 2. As indicated there, the embedded particles are about five times stiffer than the matrix and are assumed not to experience any damage, i.e., remain linearly elastic. The PUC representation is obtained after the interaction of a structured mesh with the geometrical representation of the spherical inclusions using the IGFEM methodology described in Section 3. The back planes in Fig. 4 show the structured mesh used in the analysis. The mesh is composed of 352,583 four-node tetrahedral elements, with a total of 64,404 nodes. The interaction results in the creation of 83,400 integration elements and 26,966 additional nodes along the interfaces. The problem contains a total of 266,487 degrees of freedom, with 21,600 of them with a prescribed value. The first set of simulations summarized in this section does not involve the contribution of in-plane macroscopic strains (i.e., $\varepsilon_{\alpha\beta}=0$). The results obtained hereafter are thus used as reference for those presented in the following section.

Table 2
Material properties used for the PUC problem shown in Fig. 4.

	E (GPa)	ν	$\overline{Y}$ (kPa)	p_1	p_2
Particle	20.0	0.3	–	–	–
Matrix	3.9	0.34	10	100	1

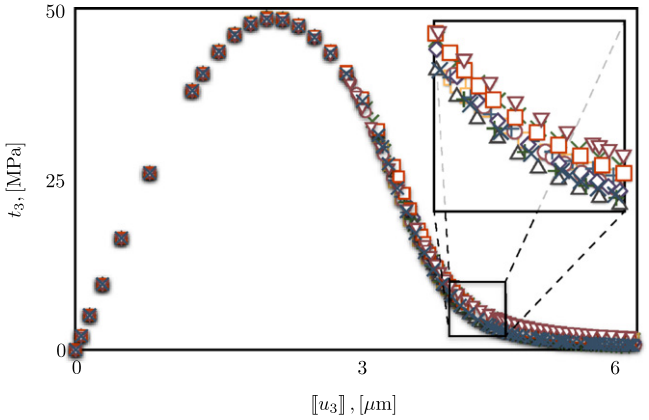

Fig. 5. Mode I traction–separation curves resulting from ten different microscopic realizations with 10% volume fraction of spherical elastic inclusions. The inset shows in detail the responses in the softening part of the curves, where the differences are most noticeable.

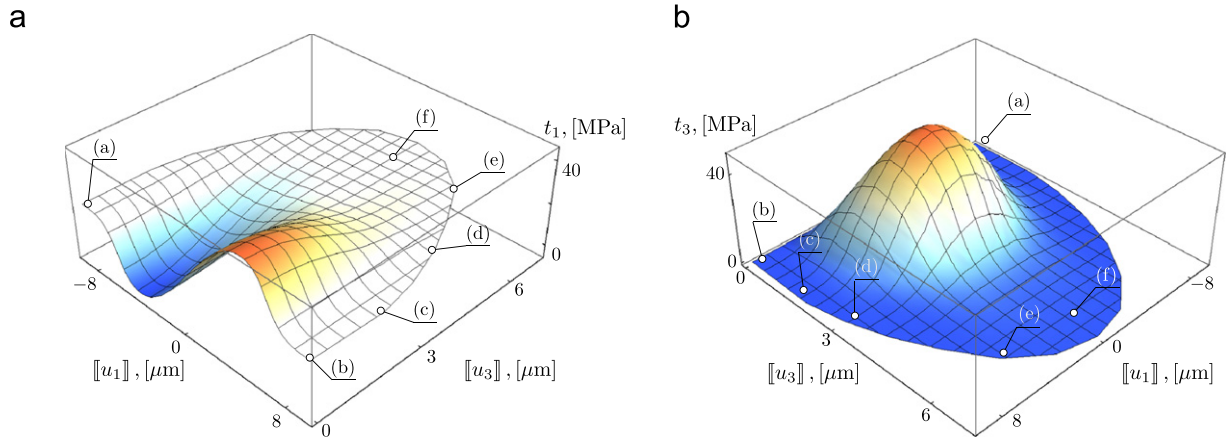

Fig. 6. Cohesive envelopes for (a) tangential cohesive traction t_1; and (b) normal cohesive traction t_3. Damage states corresponding to six points on the cohesive envelope, labeled (a)–(f), are illustrated in Fig. 7.

To investigate the impact of the particle distribution on the predicted macroscopic cohesive law, we present in Fig. 5 the mode I traction–separation curves obtained for ten particle distributions with the same volume fraction (10%). As apparent in that figure, the macroscopic curves are almost identical, with the most noticeable differences observed in the softening part of the curves, as illustrated in the inset. Based on these results, the simulations presented in the remainder of the manuscript are performed on one realization of the microstructure.

The extraction of a cohesive failure envelope is achieved by applying a linearly increasing displacement jump vector with orientations ranging from mode I to mode II, as described by the angle α in

$$\begin{aligned} [\![u_1(\tau)]\!] &= 0.4\tau\cos(\alpha),\\ [\![u_2(\tau)]\!] &= 0,\\ [\![u_3(\tau)]\!] &= 0.2\tau\sin(\alpha), \end{aligned} \tag{15}$$

where τ denotes time (given in seconds). Since the formulation is rate-dependent, care must be taken so that the same macroscopic strain rate $\dot{\varepsilon}$ is applied in both directions. As indicated by Eq. (15), $\alpha=0$ and $\alpha=\pi$ denote pure sliding modes (mode II), while $\alpha=\pi/2$ corresponds to the pure opening mode (mode I). Therefore, any other value denotes mixed-mode loading. To construct the cohesive failure envelopes, a total of 17 curves are employed with the angle α varying uniformly every $\alpha=\pi/16$ over the interval $[0,\pi]$. Each simulation is performed up to a maximum time of 1 min.

Fig. 6 presents the envelopes obtained for the microstructure shown in Fig. 4. Similarly to the two-dimensional results presented by Matouš et al. (2008), the normal and tangential traction envelopes are found to be symmetric and anti-symmetric with respect to the plane $[\![u_1]\!]=0$, respectively. Details of the failure process taking place in the PUC for six representative loading conditions (denoted (a)–(f) in Fig. 6) are presented in Fig. 7. The displacement field of the PUC is

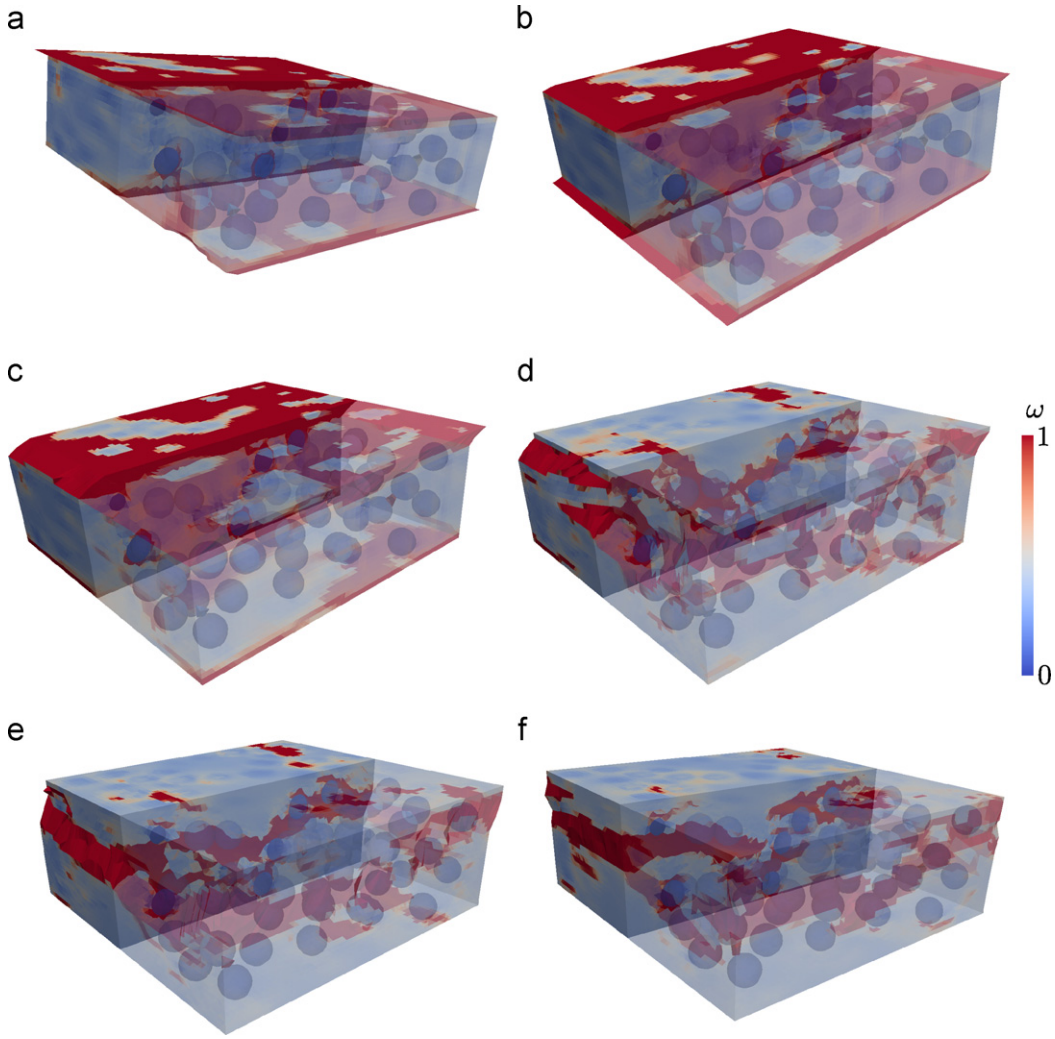

Fig. 7. Damage response for the PUC shown in Fig. 4, taken from points located on the cohesive envelopes of Fig. 6, for different values of the angle α: (a) $\alpha=\pi$; (b) $\alpha=0$; (c) $\alpha=\pi/8$; (d) $\alpha=\pi/4$; (e) $\alpha=3\pi/8$; and (f) $\alpha=\pi/2$.

magnified and half of the PUC is translucent to ease the visualization of the microstructure. The contours shown in Fig. 7a–f are those of the damage parameter ω, introduced after Eq. (4), at the end of failure process. The first two Fig. 7a and b correspond to the mode II cases and clearly show that the damage in the adhesive layer is concentrated along the top and bottom surfaces. As more tensile loading is added, culminating with the pure mode I case in Fig. 7f, the damage relocates to the interior of the adhesive layer with the particles playing the role of stress concentrators.

5. Impact of in-plane deformations on the macroscopic cohesive failure response

To investigate the effect of in-plane deformations on the macroscopic cohesive failure response of the adhesive, we apply the macroscopic deformation loading in two stages as shown in Fig. 8. In the first stage, the in-plane strain is applied with a ramp function with the same rate as before ($\dot{\varepsilon} = 1\%/\mathrm{s}$), until a maximum level is achieved at time τ_1. This in-plane strain level is then kept constant and the opening displacement jump $[\![u_3]\!]$ is applied incrementally using again a ramp function

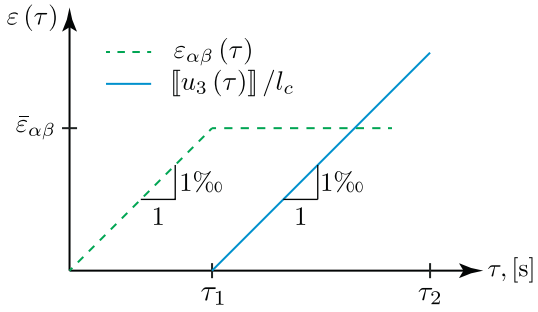

Fig. 8. Deformation loading strategy applied in two stages. In the first stage, the in-plane strain $\varepsilon_{\alpha\beta}$ is applied linearly using a ramp function until it reaches a maximum value $\bar{\varepsilon}_{\alpha\beta}$ at time τ_1. In the second stage, the deformation corresponding to a normal (mode I) displacement jump $[\![u_3]\!]$ is applied gradually with the same rate until time τ_2 at the end of the simulation.

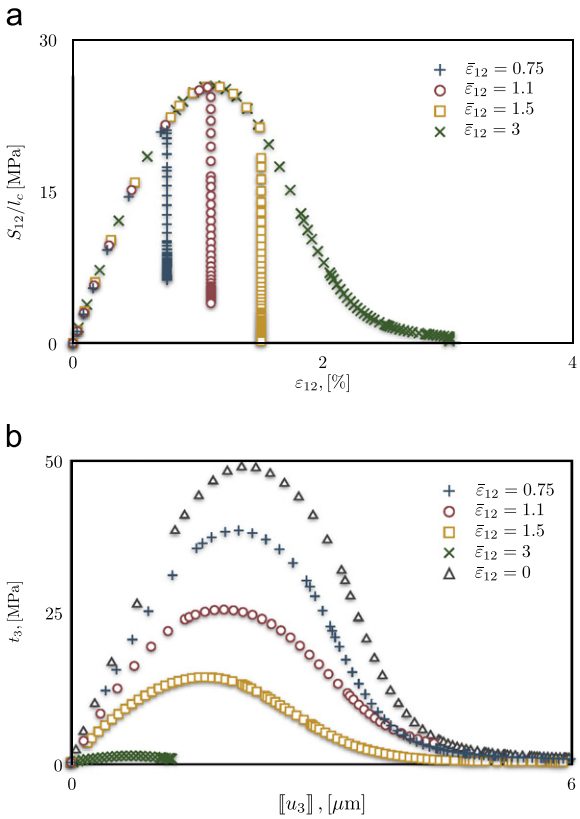

Fig. 9. (a) Homogenized in-plane shear stress S_{12} curves and (b) mode I traction–separation curves, for different values of maximum applied in-plane macroscopic shear strain $\bar{\varepsilon}_{12}$ (in %), during the two-stage loading sequence shown in Fig. 8.

until the end of the simulation at time τ_2, when complete failure of the adhesive layer is achieved. In the figure, $\varepsilon_{\alpha\beta}$ corresponds to any in-plane strain component, i.e., ε_{11}, ε_{12} or ε_{22}, or a combination thereof. Only the prescribed components of the macroscopic strain tensor discussed in each example have a nonzero value.

Fig. 9a shows the homogenized in-plane shear traction S_{12} (Eq. (8)) as a function of the applied macroscopic in-plane shear strain ε_{12} for different values of the maximum applied strain $\bar{\varepsilon}_{12}$. As indicated there, the in-plane strain is incremented until a maximum value $\bar{\varepsilon}_{12}$ is obtained, which marks the end of the first stage of the loading. After this point, the in-plane strain is kept constant as described earlier, and the decay in homogenized in-plane shear stress shows the degradation of the material due to the mode I loading in the second stage. The mode I traction–separation curves corresponding to five values of the maximum applied in-plane shear $\bar{\varepsilon}_{12}$ (which include the case $\bar{\varepsilon}_{12}=0$ for reference) are presented in Fig. 9b.

This type of analysis allows to quantify the impact of in-plane shear strain on the cohesive failure of the heterogeneous adhesives, and in particular its impact on the two key parameters that define the cohesive failure law, i.e., the fracture toughness and G_{Ic} (area under the curve) and the critical failure strength σ_c (maximum value of the cohesive traction). The

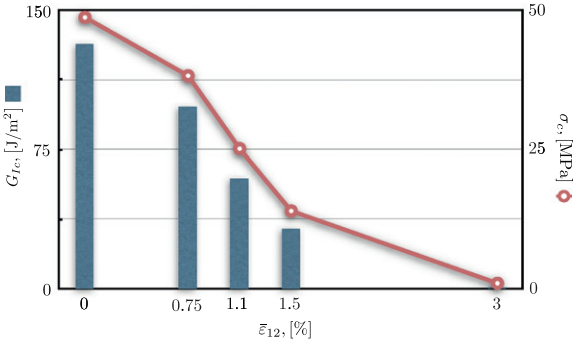

Fig. 10. Effect of the maximum in-plane shear strain $\bar{\varepsilon}_{12}$ on the fracture toughness G_{Ic} and on the critical failure strength σ_c.

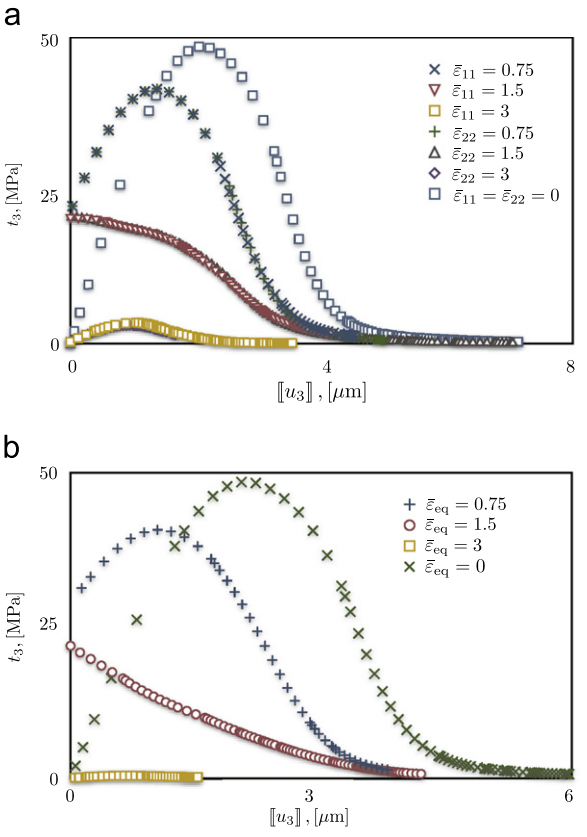

Fig. 11. Traction–separation laws for different values of maximum applied uniaxial in-plane strains $\bar{\varepsilon}_{11}$, $\bar{\varepsilon}_{22}$ (top) and equi-biaxial strain $\bar{\varepsilon}_{eq}=(\bar{\varepsilon}_{11}^2+\bar{\varepsilon}_{22}^2)^{1/2}$ (bottom) during the two-stage loading of Fig. 8. The applied in-plane strain values are given in %.

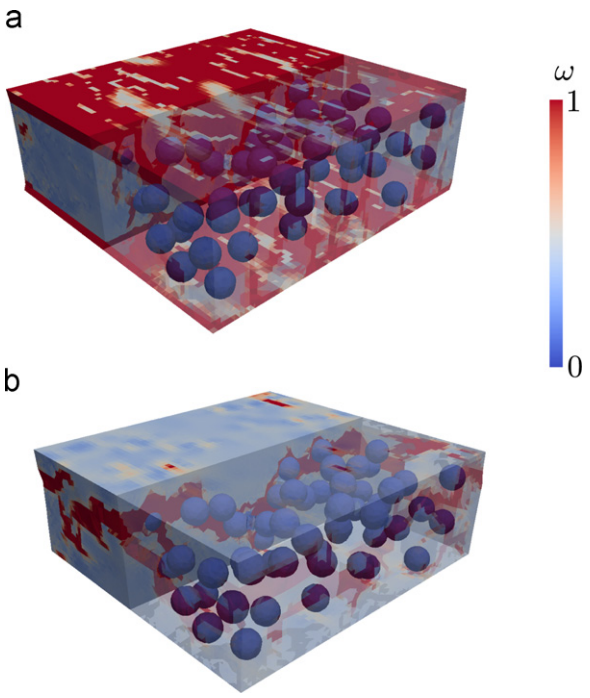

Fig. 12. Damage pattern obtained at the end of the simulation for a maximum applied uniaxial strain of (a) $\overline{\varepsilon}_{11} = 0.75\%$, and (b) $\overline{\varepsilon}_{11} = 1.5\%$.

evolution of the dependence of these two key parameters on the maximum applied in-plane shear strain $\overline{\varepsilon}_{12}$ is presented in Fig. 10, showing a strong dependence of both G_{Ic} and σ_c on the maximum applied in-plane shear strain.

Similar results are presented in Fig. 11a and b for the case of in-plane uniaxial and equi-biaxial strain loading, respectively. Unlike in the case of macroscopic in-plane shear strain showed previously (Fig. 9), for which the macroscopic shear strain applied during the first phase of the loading process did not generate out of plane stresses in the adhesive, the application of in-plane uniaxial or biaxial tensile strains lead to the introduction of out-of-plane stresses in the adhesive layer, thereby affecting the initial value of the cohesive traction t_3 at the beginning of the second loading phase. This effect is clearly apparent in Fig. 11a and b, with the cohesive mode I traction–separation curves starting from a finite value. In the uniaxial case displayed in Fig. 11a, the predicted cohesive failure curves associated with the same values of the maximum in-plane deformation ($\overline{\varepsilon}_{11}$ and $\overline{\varepsilon}_{22}$) are almost identical, pointing to the in-plane isotropy of the adopted microstructure of the adhesive layer. As was the case for the in-plane shear strain case, a relatively small value of the applied macroscopic in-plane tensile strain has a substantial impact on the predicted traction–separation law, both in terms of strength and toughness. This effect is even more pronounced for the case of equi-biaxial strain loading of the adhesive layer, as illustrated in Fig. 11b. For this loading scenario, the amplitude of the applied in-plane strains is quantified with the aid of an equivalent strain measure $\overline{\varepsilon}_{\text{eq}} = (\overline{\varepsilon}_{11}^2 + \overline{\varepsilon}_{22}^2)^{1/2}$. Finally, Fig. 12 presents details on the microscale damage pattern in the adhesive layer as obtained at the end of the two-step loading corresponding to a uniaxial applied strain $\overline{\varepsilon}_{11} = 0.75\%$ (Fig. 12a) and $\overline{\varepsilon}_{11} = 1.5\%$ (Fig. 12b). As apparent there, the smaller level of the in-plane strain ($\overline{\varepsilon}_{11} = 0.75\%$) leads to a small modification of the mode I failure pattern, which remains primarily cohesive, i.e., takes place primarily inside the adhesive layer. For the larger value of the applied macroscopic in-plane strain ($\overline{\varepsilon}_{11} = 1.5\%$), the failure pattern at the conclusion of the mode I loading process is definitely adhesive, i.e., it takes place primarily along the top and bottom surfaces of the adhesive layer.

6. Conclusion

This paper has presented a 3D micro- to macro-scale cohesive finite element framework aimed at relating damage processes taking place in a heterogeneous adhesive to the macroscopic traction–separation law that describes the failure of the bonded structure. Emphasis has been placed on capturing the impact of applied in-plane strains on the cohesive response of the adhesive. A key element of the finite element model is the IGFEM scheme used to capture accurately and efficiently the structural response of heterogeneous materials using finite element discretizations that do not conform to the material interfaces. This feature is particularly useful in the geometrically more complex 3D case studied in this manuscript, and to analyze multiple realizations of the random microstructure to extract some statistical features of the macroscopic failure law. The 3D IGFEM-based framework has been applied to model the failure of an adhesive system composed of stiff elastic particles embedded in a more compliant matrix whose failure is described by an isotropic rate-dependent damage model. The cohesive failure envelopes associated with a wide range of mode I, mode II and mixed-mode loading conditions have been extracted. Examination of the predicted failure patterns in the adhesive layer showed a transition from cohesive

failure (inside the adhesive layer) in mode I to an adhesive failure (concentrated near the adherents) under mode II conditions. The two-scale cohesive framework was then used to investigate the impact of in-plane tensile and shear strains on the predicted mode I response of the adhesive, showing a substantial influence on the failure pattern within the adhesive layer, which translates in the degradation of both its strength and fracture toughness.

Acknowledgments

The authors thank the support of the Industrial Research Institute and the National Science Foundation. Additional support was provided by the Air Force Office of Scientific Research MURI (Grant # FA9550-09-1-0686). Discussions with Dr. Mohan Kulkarni from ExxonMobil Research and Engineering are also gratefully acknowledged.

References

Babuška, I., Banerjee, U., Osborn, J.E., 2003. Survey of meshless and generalized finite element methods: a unified approach. Acta Numer. 12, 1–125, http://dx.doi.org/10.1017/S0962492902000090. arXiv:http://journals.cambridge.org/article_S0962492902000090.

Cid Alfaro, M., Suiker, A., De Borst, R., 2010. Transverse failure behavior of fiber-epoxy systems. J. Compos. Mater. 44 (12), 1493–1516, http://dx.doi.org/10.1177/0021998309360941.

Coenen, E.W.C., Kouznetsova, V.G., Geers, M.G.D., 2011. Enabling microstructure-based damage and localization analyses and upscaling. Modelling Simulation Mater. Sci. Eng. 19 (7), 074008, http://dx.doi.org/10.1088/0965-0393/19/7/074008.

Coenen, E., Kouznetsova, V., Geers, M., 2012. Novel boundary conditions for strain localization analyses in microstructural volume elements. Int. J. Numer. Methods Eng. 90 (1), 1–21, http://dx.doi.org/10.1002/nme.3298.

Dean, G., Crocker, L., Read, B., Wright, L., 2004. Prediction of deformation and failure of rubber-toughened adhesive joints. Int. J. Adhes. Adhes. 24 (4), 295–306, http://dx.doi.org/10.1016/j.ijadhadh.2003.08.002.

Ferracin, T., Landis, C.M., Delannay, F., Pardoen, T., 2003. On the determination of the cohesive zone properties of an adhesive layer from the analysis of the wedge-peel test. Int. J. Solids Struct. 40 (11), 2889–2904. URL http://dx.doi.org/10.1016/S0020-7683(03)00076-3.

Fries, T.-P., 2008. A corrected XFEM approximation without problems in blending elements. Int. J. Numer. Methods Eng. 75 (5), 503–532, http://dx.doi.org/10.1002/nme.2259.

Geubelle, P.H., Baylor, J.S., 1998. Impact-induced delamination of composites: a 2d simulation. Compos. Part B: Eng. 29 (5), 589–602. URL http://dx.doi.org/10.1016/S1359-8368(98)00013-4.

Guarino, A., Ciliberto, S., Garcimartín, A., 1999. Failure time and microcrack nucleation. EPL Europhys. Lett. 47 (4), 456. URL http://dx.doi.org/10.1209/epl/i1999-00409-9.

Hirschberger, C., Ricker, S., Steinmann, P., Sukumar, N., 2009. Computational multiscale modelling of heterogeneous material layers. Eng. Fract. Mech. 76 (6), 793–812, http://dx.doi.org/10.1016/j.engfracmech.2008.10.018.

Kawaguchi, T., Pearson, R.A., 2003. The effect of particle-matrix adhesion on the mechanical behavior of glass filled epoxies. Part 2. A study on fracture toughness. Polymer 44 (15), 4239–4247. URL http://dx.doi.org/10.1016/S0032-3861(03)00372-0.

Kinloch, A.J., 2003. Toughening epoxy adhesives to meet today's challenges. MRS Bull. 28, 445–448, http://dx.doi.org/10.1557/mrs2003.126.

Kulkarni, M.G., Geubelle, P.H., Matouš, K., 2009. Multi-scale modeling of heterogeneous adhesives: effect of particle decohesion. Mech. Mater. 41 (5), 573–583. URL http://dx.doi.org/10.1016/j.mechmat.2008.10.012.

Kulkarni, M.G., Matouš, K., Geubelle, P.H., 2010. Coupled multi-scale cohesive modeling of failure in heterogeneous adhesives. Int. J. Numer. Methods Eng. 84 (8), 916–946, http://dx.doi.org/10.1002/nme.2923.

Matouš, K., Kulkarni, M.G., Geubelle, P.H., 2008. Multiscale cohesive failure modeling of heterogeneous adhesives. J. Mech. Phys. Solids 56 (4), 1511–1533, http://dx.doi.org/10.1016/j.jmps.2007.08.005.

McBride, A., Mergheim, J., Javili, A., Steinmann, P., Bargmann, S., 2012. Micro-to-macro transitions for heterogeneous material layers accounting for in-plane stretch. J. Mech. Phys. Solids 60 (6), 1221–1239. URL http://dx.doi.org/10.1016/j.jmps.2012.01.003.

Meguid, S.A., Sun, Y., 2004. On the tensile and shear strength of nano-reinforced composite interfaces. Mater. Des. 25 (4), 289–296, http://dx.doi.org/10.1016/j.matdes.2003.10.018.

Needleman, A., 1990. An analysis of decohesion along an imperfect interface. Int. J. Fract. 42, 21–40, http://dx.doi.org/10.1007/BF00018611.

Nguyen, V.P., Lloberas-Valls, O., Stroeven, M., Sluys, L.J., 2011. Homogenization-based multiscale crack modelling: from micro-diffusive damage to macro-cracks. Comput. Methods Appl. Mech. Eng. 200 (9–12), 1220–1236, http://dx.doi.org/10.1016/j.cma.2010.10.013.

Nguyen, V.P., Lloberas-Valls, O., Stroeven, M., Sluys, L.J., 2012. Computational homogenization for multiscale crack modeling. Implementational computational aspects. Int. J. Numer. Methods Eng. 89 (2), 192–226, http://dx.doi.org/10.1002/nme.3237.

Ortiz, M., Pandolfi, A., 1999. Finite-deformation irreversible cohesive elements for three-dimensional crack-propagation analysis. Int. J. Numer. Methods Eng. 44 (9), 1267–1282, http://dx.doi.org/10.1002/(SICI)1097-0207(19990330)44:9 < 1267::AID-NME486 > 3.0.CO;2-7.

Ramanathan, S., Ertaş, D., Fisher, D.S., 1997. Quasistatic crack propagation in heterogeneous media. Phys. Rev. Lett. 79, 873–876, http://dx.doi.org/10.1103/PhysRevLett.79.873.

Simo, J., Ju, J., 1987a. Strain- and stress-based continuum damage models—i. Formulation. Int. J. Solids Struct. 23 (7), 821–840, http://dx.doi.org/10.1016/0020-7683(87)90083-7.

Simo, J., Ju, J., 1987b. Strain- and stress-based continuum damage models—ii. Computational aspects. Int. J. Solids Struct. 23 (7), 841–869, http://dx.doi.org/10.1016/0020-7683(87)90084-9.

Soghrati, S., Geubelle, P.H., 2012. A 3d interface-enriched generalized finite element method for weakly discontinuous problems with complex internal geometries. Comput. Methods Appl. Mech. Eng. 217–220, 46–57. URL http://dx.doi.org/10.1016/j.cma.2011.12.010.

Soghrati, S., Aragón, A.M., Armando Duarte, C., Geubelle, P.H., 2011. An interface-enriched generalized FEM for problems with discontinuous gradient fields. Int. J. Numer. Methods Eng. http://dx.doi.org/10.1002/nme.3273.

Stafford, D.S., Jackson, T.L., 2010. Using level sets for creating virtual random packs of non-spherical convex shapes. J. Comput. Phys. 229 (9), 3295–3315, http://dx.doi.org/10.1016/j.jcp.2010.01.003.

Tang, C., Kou, S., 1998. Crack propagation and coalescence in brittle materials under compression. Eng. Fract. Mech. 61 (3–4), 311–324, http://dx.doi.org/10.1016/S0013-7944(98)00067-8.

White, S.R., Sottos, N.R., Geubelle, P.H., Moore, J.S., Kessler, M.R., Sriram, S.R., Brown, E.N., Viswanathan, S., 2001. Autonomic healing of polymer composites. Nature 409 (6822), 794–797. URL http://dx.doi.org/10.1038/35057232.

Zhao, Q., Hoa, S.V., 2007. Toughening mechanism of epoxy resins with micro/nano particles. J. Compos. Mater. 41 (2), 201–219, http://dx.doi.org/10.1177/0021998306063361. arXiv:http://jcm.sagepub.com/content/41/2/201.full.pdf+html.

Zhao, W., Ramani, K., Mueller, B.E., 2000. Processing and fracture behavior of a polyethylene-based thermoplastic adhesive and a glass–fiber filled epoxy adhesive. Int. J. Adhes. Adhes. 20 (5), 409–413, http://dx.doi.org/10.1016/S0143-7496(99)00065-2.